Chapter 3 Magnetic Ground State of $BaFe_{12}O_{19}$: Evidence for Noncollinear Magnetic Structure and Incommensurate Conical Modulation

3.1 Introduction

As discussed in chapter 1, the hexaferrites are technologically important and commercially used materials for a variety of applications such as permanent magnets, gyromagnetic devices, high-speed digital electronics, telecommunication, radar and energy generation [12,13,117,193]. Among the M, Y, W, Z, X and U-type of hexaferrites, recent years have witnessed a spurt of interest in Y [2,5,103,112] and Z-type [1,4,105] hexaferrites due to the discovery of type-II multiferroicity near the room temperature on account of conical magnetic structure in which the magnetic moments precesse about a specific crystallographic direction [96,112], a brief account of which has already been presented in chapter 1. Y and Z-type hexaferrites exhibit longitudinal conical ordering in which the magnetic moments precesse about the c-axis. This has been confirmed by the observation of characteristics magnetic satellite peaks along the *hhl* reciprocal lattice rows around $l = 2n \pm 1$ positions. These satellite peaks are otherwise forbidden by the nuclear and collinear magnetic structures [3,101]. On application of a magnetic field transverse to the c-axis, the conical ordering in these compounds changes from longitudinal (// c-axis) to transverse ($\perp$ c-axis) and the magnetic moments now precesse about an axis perpendicular to the c-axis [29,94,96]. This field-induced longitudinal to transverse conical ordering transition is at the heart of the type-II magnetoelectric coupling through the inverse Dzyaloshinskii-Moriya (DM) interaction [3,111,194,195] as discussed in chapter 1.

The M-type hexaferrites, like barium hexaferrite $BaFe_{12}O_{19}$ (BFO), have all along been believed to possess collinear magnetic structure with moments aligned along the c-axis as per the classic Gorter model [39]. The spin configuration for this model is shown schematically in Fig. 3.1(a). Since M-type hexaferrites occupy the major market share among the different hexaferrites, there is considerable interest in discovering conical magnetic ordering [29,132,133] and hence type-II multiferroicity in this family of hexaferrites also. In this context, it has been known that Sc doping in $BaFe_{12}O_{19}$ and $SrFe_{12}O_{19}$ induces longitudinal conical magnetic ordering whose cone angle about the c-axis increases with increasing Sc concentration [132,133]. More interestingly, these doped compositions have recently been shown to exhibit type-II multiferroicity with record-high ferroelectric polarization of ~25 $\mu C/m^2$ under transverse magnetic field [29].

Since the existence of type-II magneto-electric coupling in hexaferrites is intimately linked with the existence of the conical magnetic order, it is of immense interest to search for conical ordering in undoped M-type hexaferrite also. With this objective in mind, this chapter presents the results of X-ray absorption spectra (XAS), X-ray magnetic circular dichroism (XMCD) and neutron diffraction studies on single-crystals of BFO at $T \lesssim 1.5$ K to understand its magnetic ground state. Our XAS and XMCD studies at the Fe $L_{2,3}$-edges confirm the non-collinear magnetic structure of BFO at ~ 1.2 K. Our single-crystal neutron diffraction studies at ~ 1.5 K confirm conical magnetic order as revealed by the presence of magnetic satellite peaks along the *00l* reciprocal lattice row around the $l = 2n \pm 1$ positions, which are otherwise forbidden by the nuclear $P6_3/mmc$ [131] and the magnetic $P6_3/mm'c'$ [15,131] space groups. Besides presenting the experimental details and results of our XAS, XMCD and neutron diffraction, a brief summary of the current understanding of XAS spectra at the Fe $L_{2,3}$-edges along with the understanding of XMCD signals of Fe at the $L_{2,3}$-edges is also included in this chapter.
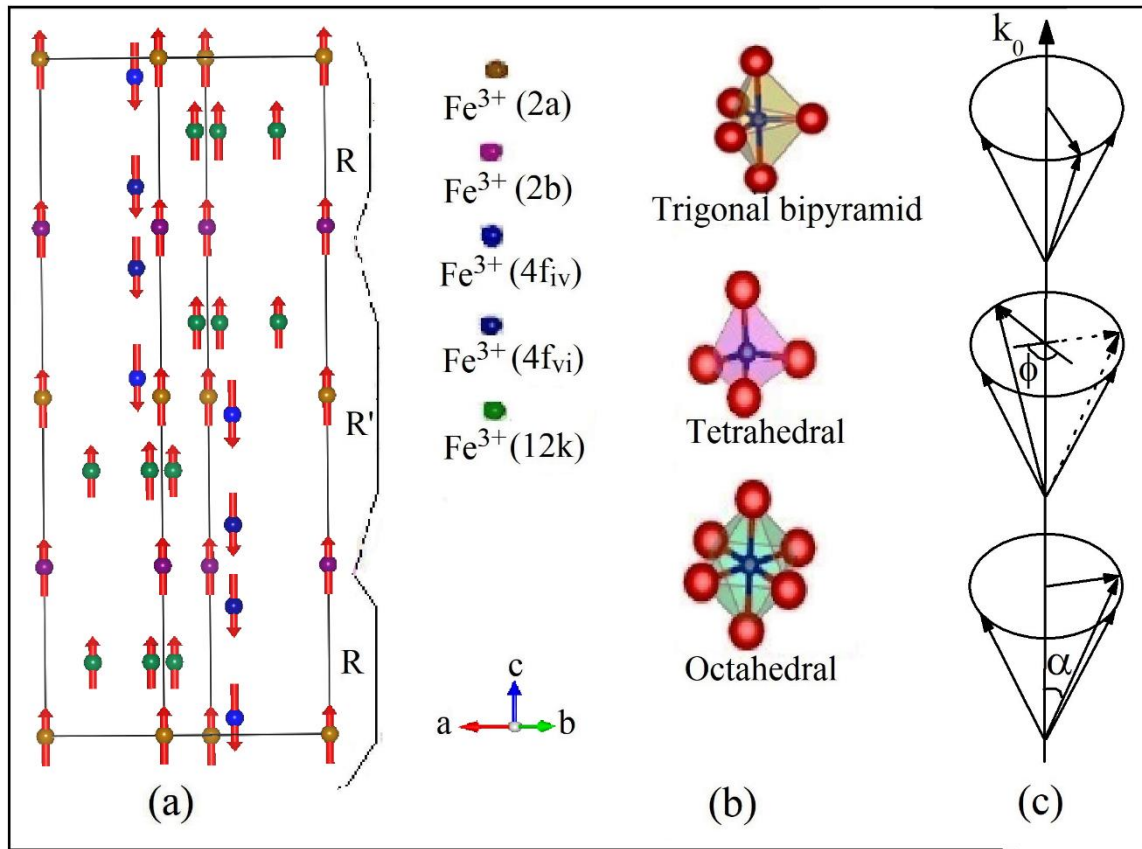
Figure 3.1: Schematic representation of (a) collinear magnetic structure of $BaFe_{12}O_{19}$, (b) coordination polyhedra for Fe^{3+} ions in $BaFe_{12}O_{19}$ and (c) longitudinal conical magnetic structure due to precession of the net moment in the R and R′ blocks about the c-axis for canted spins.

3.2   Current Understanding of the XAS Spectra at the Fe L$_{2,3}$-edges

The X-ray absorbing capacity of a material is usually explained in terms of the Beer-Lambert's law which can be stated as [196,197]:

$$I_t = I_0 e^{-\mu t} \qquad \qquad \text{…….(3.1)}$$

where I_0 is the intensity of incident electromagnetic radiation, t is the thickness of the target material, I_t is the intensity of the beam after passing through the sample and μ is the linear absorption coefficient This coefficient (μ) is a material-specific quantity and is directly related to the absorption cross-section of the sample under consideration. Further, when we measure the absorption signals by varying the energy of the incident X-ay beam,

we observe several absorption steps in the absorption spectrum. These absorption steps are simply absorption edges that correspond to the binding energy of the core electrons. In general, one observes three absorption edges, namely K, L and M-edges, which arise due to the transition of the electrons from shell with n = 1 (K-shell i.e., 1s orbital), 2 (L-shell i.e., 2s and 2p orbitals), and 3 (M-shell i.e., 3s, 3p and 3d orbitals) to the unoccupied shells. It is well known that the L and M-edges split into 3 (i.e., L_1, L_2, and L_3) and 5 (i.e., M_1, M_2, M_3, M_4, and M_5) levels, respectively, due to the spin-orbit coupling [196,197]. To a first approximation, the dipole selection rule for X-ray absorption is $\Delta l = \pm 1$. The excitation of the electrons from 2s and 2p (i.e., L-shell) to the unoccupied 3p and 3d-levels lead to L_1, L_2, and L_3-edges, respectively. Since $L_{2,3}$-edges involve the transition of core electron to unoccupied 3d-levels, a study of the absorption spectrum at the $L_{2,3}$-edges is the best probe to explore the d-orbital properties like magnetic and optical properties of transition metals like iron (Fe).

XAS is an element-specific technique and frequently used to probe the electronic structure and local geometry of the metals in a variety of systems [198,199]. The transition-metals in most of the compounds such as spinels, garnets, perovskites and hexaferrites are located in the octahedral, tetrahedral and trigonal bipyramid environments created by oxygen anions. A doublet peak at the L_3 as well as the L_2-edges of Fe are observed in the XAS spectra of the oxides, spinels and hexaferrites. Fig. 3.2 depicts the typical XAS spectra at the Fe $L_{2,3}$-edges of compounds, such α-Fe_2O_3, $GaFeO_3$, γ-Fe_2O_3, perovskite $LaFeO_3$, Y-type hexaferrite $Ba_{0.5}Sr_{1.5}Zn_2Fe_{12}O_{22}$ and M-type hexaferrite $SrFe_{12}O_{19}$. It is evident from these figures that the doublet profile at the L_3-edge is more often centred around 710 eV except for the Y-type hexaferrites where it is centred at ~ 705 eV (see Fig. 3.2 (e)). For the three different oxygen environments (octahedral (OH), tetrahedral (TH) and trigonal bipyramid (TBP)) present in the M-type
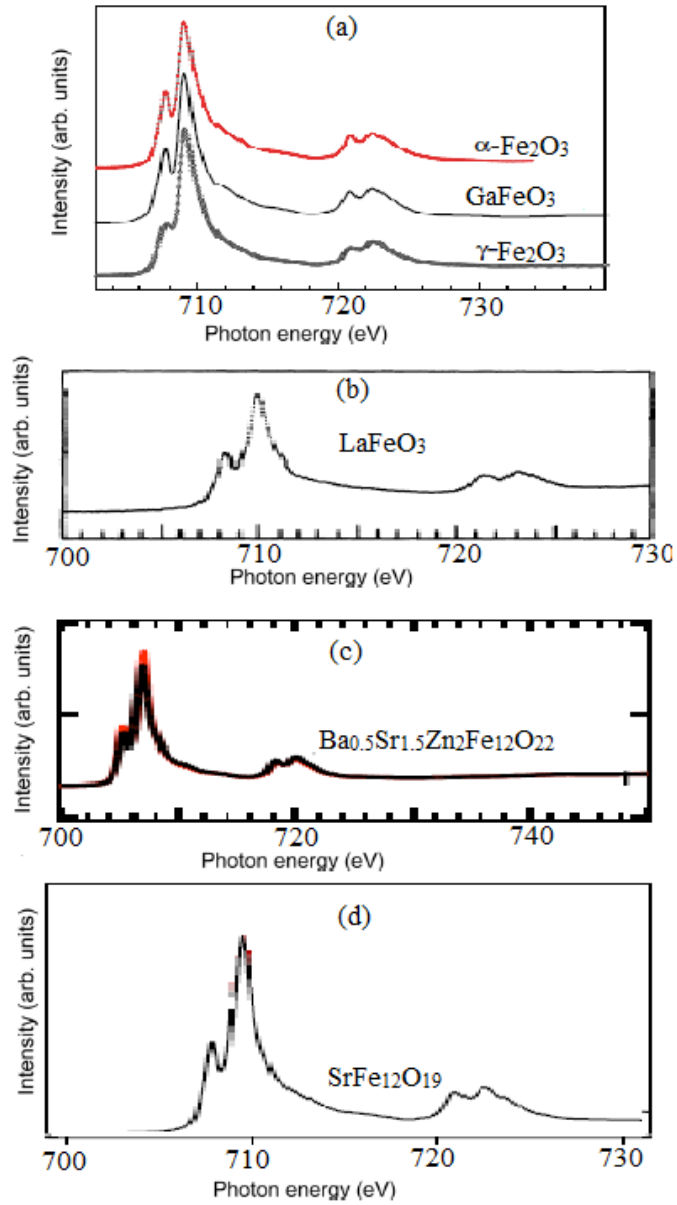
Figure 3.2: XAS spectra of (a) α-Fe_2O_3, $GaFeO_3$ and γ-Fe_2O_3 [200,201], (b) $LaFeO_3$ [201], (c) $Ba_{0.5}Sr_{1.5}Zn_2Fe_{12}O_{22}$ [6] and (d) $SrFe_{12}O_{19}$ [202] at the Fe $L_{2,3}$-edges.

hexaferrite $SrFe_{12}O_{19}$, the theoretically simulated XAS spectra at the Fe $L_{2,3}$-edges using atomic multiplet calculations are depicted in Fig. 3.3. It is evident from this figure that XAS spectra of Fe in the OH, TH and TBP environments have similar profile with small variations in the intensity. It is also evident that the XAS spectra at the Fe L_3-edge are centred around 710 eV for all the three environments as observed experimentally in various compounds.
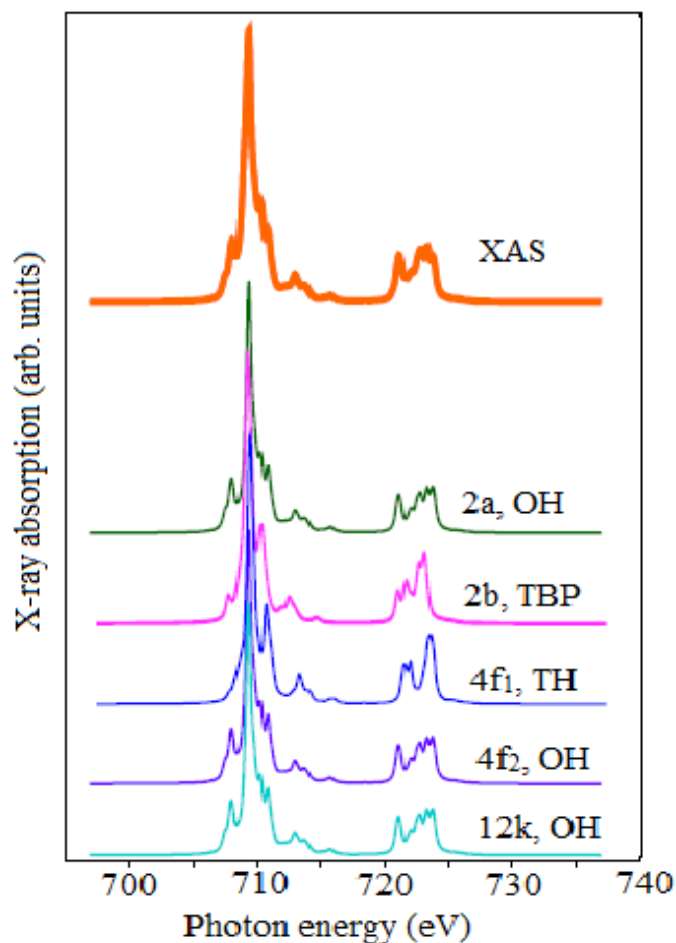
Figure 3.3: Atomic multiplet calculation based simulation of XAS spectra at the $L_{2,3}$-edges of Fe at different Wyckoff position in $SrFe_{12}O_{19}$ [202] with octahedral (OH), trigonal bipyramid (TBP) and tetrahedral (TH) environments.

3.3 Current Understanding of X-ray Magnetic Circular Dichroism (XMCD) at the Fe L$_{2,3}$-edges

XMCD technique utilizes the difference in the spin-polarized photoelectrons in the absorption process using left and right circularly polarised X-ray beams. The study of XMCD signals extracted from the XAS spectra of Fe at the $L_{2,3}$-edges enables us to estimate the ordered spin moments in ferromagnetic and ferrimagnetic materials. The study of X-ray magnetic linear dichroism (XMLD), on the other hand is better suited for investigating the antiferromagnetic materials. In the ferro/ferrimagnetic materials, the 3d valence band splits into spin-up and spin-down sub-bands due to exchange interaction as

54

proposed by Stoner [203,204]. The schematic diagram of the splitting of the 3d valence

band following the Stoner model is shown in Fig. 3.4. The valence bands represented in

blue and yellow colour are occupied by the up and down spins, respectively. Since the

number of up-spin electrons in the blue coloured valence band is higher (estimated by

area of coloured region) than down-spin electrons in yellow coloured valence band, the

net magnetization is in an upward direction. Right circularly polarised (RCP) light

transfers +ℏ momentum to the up-spin electrons and excites them to unoccupied valence

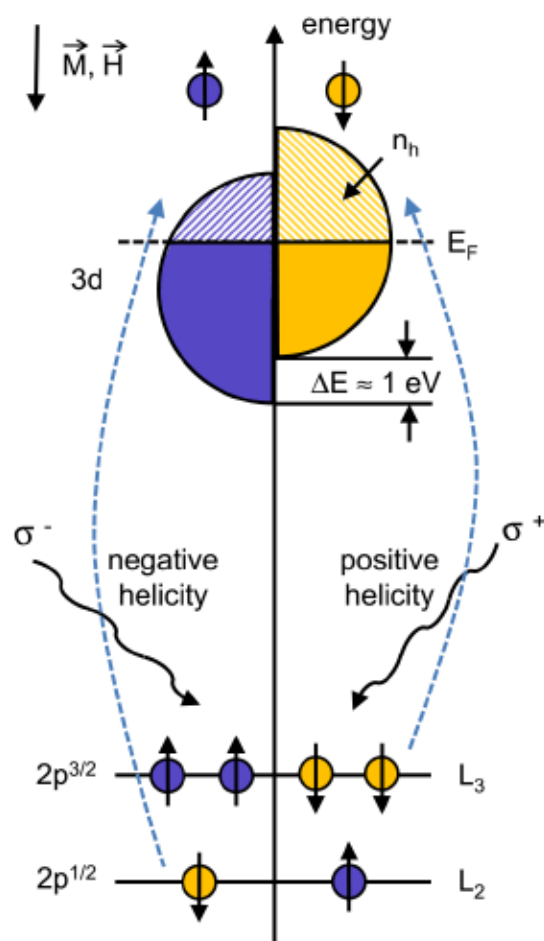bands while left circularly polarised (LCP) light transfers -ℏ momentum and excites the

Figure 3.4 The Stoner model for the splitting of 3d valence band of transition metal in
ferro/ferrimagnetic materials [205].

down-spin electrons to unoccupied valence bands. It is evident from Fig. 3.4 that absorption of the RCP light will be very small in comparison with the absorption of LCP light because of the huge unoccupied density of states in the down-spin 3d valence band than in unoccupied density of states in the up-spin 3d valence band. The difference between the absorption signal of RCP and LCP X-ray beam, i.e., the XMCD signal is used further to estimate the magnitude of the spin moments. Experimental observations suggest that shape of the XMCD signal provides information about the contributions from the Fe in the TBP, TH or OH environments. To illustrate this, the XMCD signal at the Fe L_3-edge of γ-Fe_2O_3, $GaFeO_3$, $CoFe_2O_4$ and $SrFe_{12}O_{19}$ compounds are shown in Figs. 3.5 (a) to (d), respectively. The two large valleys in the XMCD signal are attributed to the
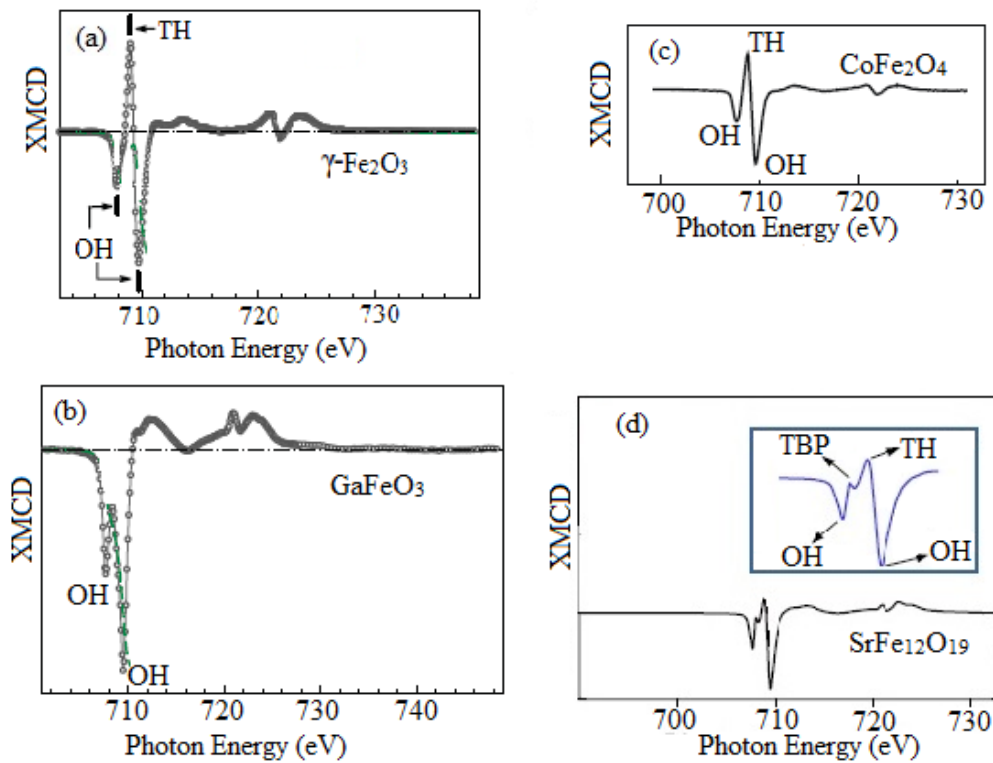

Figure 3.5: XMCD signal at the Fe L-$_{3,2}$-edges measured in the (a) γ-Fe_2O_3 [206], (b) $GaFeO_3$ [200], (c) $CoFe_2O_4$ [207] and (d) $SrFe_{12}O_{19}$ [202]. OH, TPB and TH stand for octahedral, trigonal bipyramid and tetrahedral, respectively.

iron present in the OH environment while the prominent peak for all the compounds, except for $GaFeO_3$, is attributed to TH environment. Since $GaFeO_3$ ferrite does not have TH site, the representative peak for TH environment is not present in its XMCD signal (see Fig. 3.5(b)). In all other compounds γ-Fe_2O_3, $CoFe_2O_4$ and $SrFe_{12}O_{19}$, Fe is surrounded by octahedral and tetrahedral oxygen environments and that is why XMCD signals at the Fe L_3-edge show valleys (~ 707.5 eV and ~ 709.5 eV) along with a peak (~ 709 eV) characteristic of the two environments, respectively. Further in $SrFe_{12}O_{19}$ hexaferrite, Fe ion is located in the TBP environment also along with OH and TH. A careful observation of the XMCD profile (see Fig. 3.5(d)) at the Fe L_3-edge of $SrFe_{12}O_{19}$ suggests that it has an additional peak at ~708 eV along with two valleys due to OH and one strong peak due to TH. This peak at ~708 eV in the XMCD signal was initially attributed to Fe in the TBP environment. Since this peak is observed in the XMCD signal of compounds like γ-Fe_2O_3, $GaFeO_3$ and $CoFe_2O_4$ which do not have trigonal bipyramid site (see Figs. 3.5(a) to (c)). However, this assignment is tentative as discussed in [202] and also later in section 3.5.1. We have listed the energy for the valleys and peaks in the XMCD profile at the Fe L_3-edge for $SrFe_{12}O_{19}$ shown in Figs. 3.5(d) in Table 3.1.

The theoretically computed, XMCD profiles for the L_3-edge of Fe located at the different Wyckoff sites and environments in $SrFe_{12}O_{19}$ are shown in Fig. 3.6. Fe at 2a, $4f_2$ and 12k Wyckoff sites in $SrFe_{12}O_{19}$ has OH environment of oxygen. Fig. 3.6 reveals that

Table 3.1: Energy of valleys and peaks in experimentally observed XMCD at the Fe L_3-edge for $SrFe_{12}O_{19}$ [202].

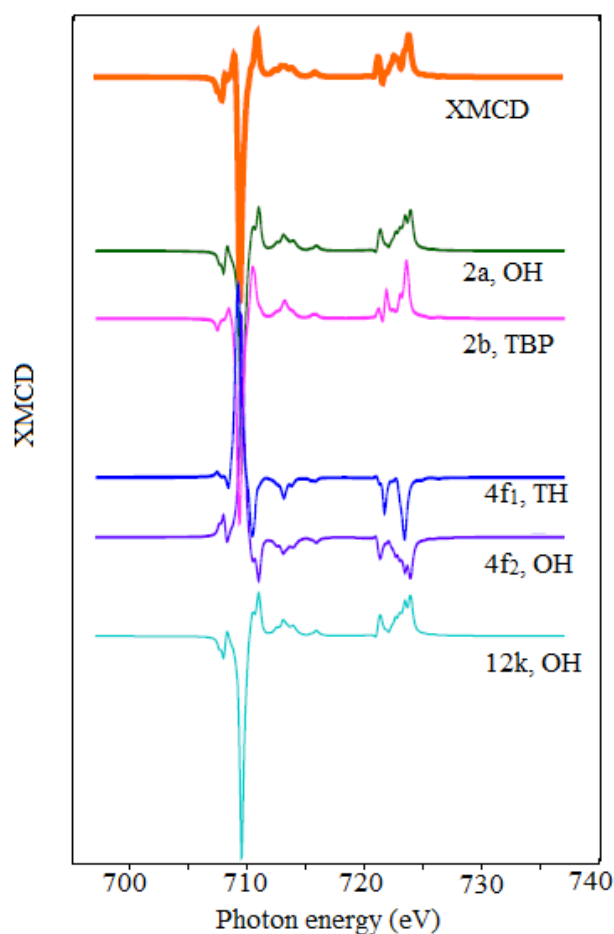| Fe environments	Valleys	Peaks
OH	~707.5 eV, 709.5 eV	--
TH	--	~ 709 eV

Figure 3.6: XMCD spectra at the Fe $L_{2,3}$-edges calculated for each iron cation of SrFe$_{12}$O$_{19}$ [202]. OH, TPB and TH stand for octahedral, trigonal bipyramid and tetrahedral, respectively.

the calculated XMCD profile for Fe at the 12k and 2a sites shows a large valley at ~ 709.5 eV and while that at 4f$_2$ site shows a prominent peak at the same energy. Since Fe at the 12k and 4f$_2$ sites have inverse characteristics, one could observe a peak at ~ 709.5 eV also instead of a valley due to Fe at 4f$_2$ site in OH environment. The simulation of the overall XMCD profile taking into account the occupation of Fe at various Wyckoff sites, however, suggests that around the L$_3$-edge it should show two valleys and a number of peaks. The approximate energy of experimentally observed peaks and valleys for each

environment at different Wyckoff sites and the corresponding prominent peaks and valleys in the overall simulated XMCD profile (see Fig. 3.6) of Fe at the L_3-edge are listed in Tables 3.1 and 3.2, respectively. The peak at ~ 708 eV in the overall XMCD profile although corresponds to the calculated energy for Fe in TBP environment in $SrFe_{12}O_{19}$ but its assignment is somewhat controversial as discussed later in section 3.5.1.

Table 3.2: Energy of valleys and peaks at the Fe L_3-edge of calculated XMCD profiles of $SrFe_{12}O_{19}$ [202].

Fe Environments / Wyckoff site	Valleys	Peaks
OH (2a)	~707.5 eV, 709.5 eV	~ 710.5 eV, 711eV
OH (12k)	~707.5 eV, 709.5 eV	~ 710.5 eV, 711eV
OH ($4f_2$)	~710.5 eV, ~711 eV	~707.5 eV, ~709.5 eV
TH ($4f_1$)	~ 707.5 eV, ~710.5 eV	~709.5 eV
TBP (2b)	~709.5 eV	~ 708 eV, ~ 710.5 eV

3.4 Experimental

Single-crystals of BFO were grown by a high-temperature solution method the details of which are given in chapter 2.

The XAS spectra at the Fe $L_{2,3}$-edges were recorded at the beam-line P04 of PETRA-III, Hamburg, Germany, using the low-temperature setup described by Beeck et al [208]. XAS measurements on single-crystals of BFO were carried out in two different geometries (the normal incidence (NI) and grazing incidence (GI)) without magnetic field at 1.2 K using RCP and LCP X-ray beams. In the NI geometry, the propagation vector (**k**) of RCP and LCP soft X-ray beam was kept parallel to the c-axis of unit cell i.e., **k**//c-axis while in the GI geometry, the **k**-vector of the incident X-ray beam makes an angle of 15^0 with respect to the c-axis of the crystal. The XAS measurements in the GI geometry were

also carried out in the presence of a magnetic field of 0.5 T applied along the beam propagation vector (**k**). To get XAS spectra, we measured the dark current from all the channels after closing the sample chamber properly. The intensity of the incoming beam (I_0) was measured using a gold mess. The charging current, i.e., drain current, of the sample was measured using a gold mess in the total electron yield (TEY) mode. To eliminate the effect of the dark signal, i.e., noise count due to the electronics, the dark count was subtracted from I_0 and drain count. The drain counts thus obtained were divided by I_0 which gives one XAS spectra. To remove any ambiguity in recorded XAS spectra, we averaged out over multiple XAS spectra measured using the LCP beam as well as the RCP beam. The averaged XAS spectra collected using the LCP and RCP beams are used for further analysis.

Single-crystal neutron diffraction measurements were carried out using WISH time-of-flight diffractometer at ISIS, United Kingdom, the details of which are given elsewhere [209].

The direct current (dc) magnetization versus magnetic field (M-H) hysteresis curves were recorded at 2 K for field H // c and H $\perp$ c using a physical properties measurement system (PPMS, DynaCool, Quantum Design, USA).

3.5   Results and Discussion

3.5.1   XAS and XMCD Study at the Fe $L_{2,3}$-edges at 1.2 K

To capture the departure from the Gorter model of the collinear magnetic structure of BFO, we have used the XMCD technique which not only probes the spin moment of the sample directly but also provides information about the direction of the magnetic moment [210–214]. In BFO, partially filled d-orbitals of the Fe^{3+} ions are responsible for the spin moment. Information about the 3d-orbital can be extracted by measuring the XAS of Fe at the L-edge, through the Fe-2p $\rightarrow$Fe-3d excitation, which

splits into L_2 and L_3-edges due to strong spin-orbit coupling. To check whether the spins are canted away from the c-axis, we obtained XMCD signals by measuring the XAS spectra over the $L_{2,3}$ energy range using LCP and RCP X-ray beams in both NI and GI geometries.

To get XMCD signals from the XAS spectra, we fit a linear background in the pre-edge region (700 eV – 704 eV) and then extrapolate it to full energy range (700 eV – 733 eV) and subtract it from the XAS spectra (σ_+) measured using the RCP X-ray beam. A similar linear background of the same slope was subtracted from XAS spectra (σ_-) measured using the LCP beam. The XAS spectra σ_+ and σ_- measured in NI geometry without field along with a linear background fit are shown in Fig. 3.7(a). After background subtraction, the post edge (730 eV – 733 eV) of σ_+ and σ_- spectra were normalized to 1. Normalized XAS spectra thus obtained and their difference $\Delta\sigma = (\sigma_+ - \sigma_-)$, which represent the XMCD signal over the $L_{2,3}$ energy range, are depicted in Figs. 3.7(b) and (c), respectively. The XAS spectra at the Fe $L_{2,3}$-edges consist of two groups; the first group (i.e., 705eV to 715eV) consists of two peaks due to the L_3-edge (Fe-$2p_{3/2}$ $\rightarrow$Fe-3d excitation) while the second group (i.e., 720 eV to 725 eV) which also consists of two peaks is due to the L_2-edge (Fe-$2p_{1/2}$ $\rightarrow$Fe-3d excitation). The L_3-edge spectra of iron has three components coming from the Fe at TBP, TH and OH site. Therefore, XMCD signal at Fe L_3-edge shows prominent characteristic features such as a valley at ~ 707.4 eV, peaks at ~707.8 eV and ~ 708.4 eV, and a large valley at ~ 709.34 eV. A comparison of the shape and energy of peaks/valleys in the XMCD signal at the Fe L_3-edge reported in literature for $SrFe_{12}O_{19}$ (see Table 3.1 and 3.2) suggests that prominent peak at ~ 708.4 eV arises due to the Fe ion at TH site while large valley at ~ 709.34 eV arises from the Fe at OH site [200,202]. In present case the prominent peak at ~ 708.4 eV in XMCD profile is due to Fe at TH site which has appeared at slightly lower energy in
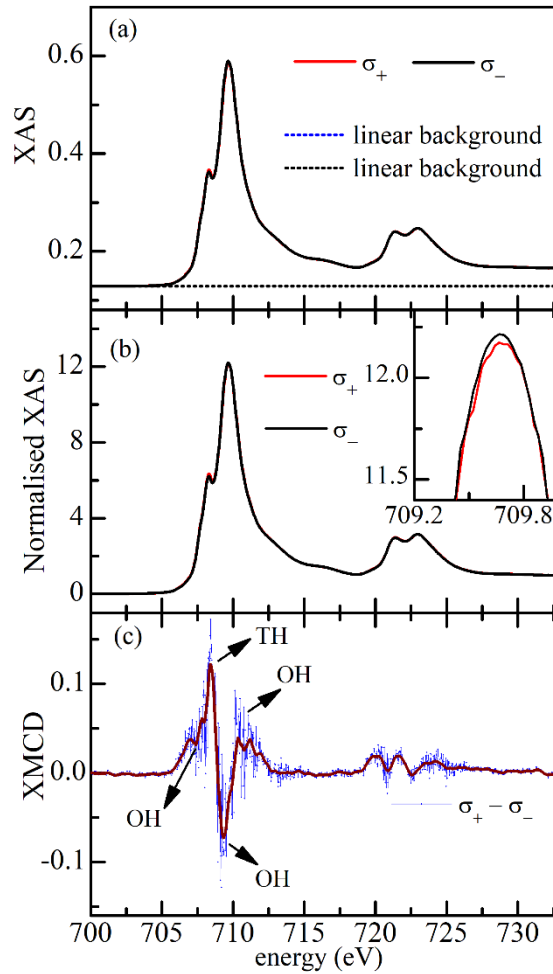
Figure 3.7: (a) XAS spectra recorded at the Fe $L_{2,3}$-edges measured at 1.2 K on a single-crystal of $BaFe_{12}O_{19}$ in NI geometry using right (σ_+) and left (σ_-) circularly polarised X-ray beams. The dotted lines represent the linear background. (b) Normalised XAS spectra and (c) XMCD signal. OH and TH in (c) is stand for octahedral and tetrahedral environments.

comparison with reported energy ~ 709 eV. Although the peak at ~ 707.8 eV can be assigned to TBP environment based on theoretical calculations [202], there are several arguments that do not allow this assignment. A peak at ~ 708.0 eV has been observed in compounds like maghemite and ferrihydrite [215,216] also where there is no Fe in the TBP environment. Further, there is only one Fe per formula unit of BFO and therefore its contribution, if any, may be negligible [202]. Finally, simulation of the XMCD profiles,

using theoretically calculated profiles for each environments of Fe for $SrFe_{12}O_{19}$, without considering the contribution of the TBP environment, also gives a peak at the same energy [202]. We therefore have assigned the peak and valley at ~ 708.4 eV and ~ 709.34 eV only to the TH and OH environments, respectively. Further, a comparison of the energy of the small valley at ~ 707.4 eV and the peak at ~ 711 eV observed in XMCD profile with those listed in Table 3.2 suggests that the valley at ~ 707.4 eV and the peak at ~ 711 eV are due to Fe in OH environment. Further, the peak at ~ 709 eV corresponds to the energy of the TH environment as can be seen from Table 3.2.

Following the same procedure, σ_+ and σ_- spectra along with a linear background fit, normalised XAS spectra and XMCD signal were obtained in the GI geometry also. These are shown in Figs. 3.8(a)-(c) and Figs. 3.9(a)-(c) without and with field 0.5 T dc bias field applied in the beam direction, respectively. It is evident from Fig. 3.8(c) that the XMCD signal in the GI geometry with zero field shows a peak at ~ 709.5 eV while under a field of H = 0.5 T, a second peak at ~ 708.2 eV gets resolved (see Fig. 3.9(c). The shape of the peak at ~ 709.5 eV in XMCD signal is reversed with respect to XMCD signal measured in the NI geometry (see Fig. 3.7(c)) which shows a large valley at around the same energy. Since there is no simulation of the XAS and XMCD profiles available for the GI geometry, we are not in a position to comment on this profile shape inversion. We, however, note that the energy of the peak coincides with that expected for the OH environment. The main conclusion we can draw from the significant XMCD signal in the GI geometry, which is enhanced substantially under dc bias a 0.5 T, is that the magnetic moments are canted away from the c-axis and therefore BFO has a non-collinear magnetic structure at 1.2 K.

The magnitude of the spin moment can be estimated using the well-established sum rule [211,217–219]:

$$m_{spin} + 7m_T^\theta = -\frac{(6P-4Q)}{R}n_h, \qquad\qquad \ldots\ldots(3.2)$$

where, $P = \int_{L_3}(\sigma_+ - \sigma_-)d\omega$ represents the integration of XMCD signal over the energy range of L_3-edge, $Q = \int_{L3+L2}(\sigma_+ - \sigma_-)d\omega$ represents the integration of the XMCD signal over the energy range of $L_{2,3}$-edges, and $R = \int_{L3+L2}(\sigma_+ + \sigma_-)d\omega$ represents the integration of the sum of XAS signal over the energy range of $L_{2,3}$-edges, m_{spin} is the spin
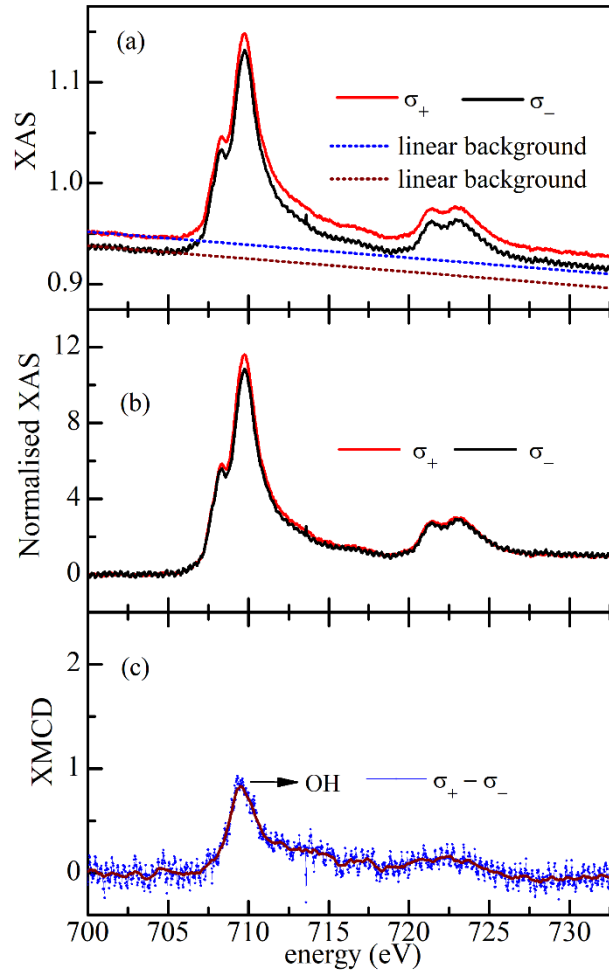

Figure 3.8: (a) XAS spectra recorded at the Fe $L_{2,3}$-edges measured at 1.2 K on a single-crystal of $BaFe_{12}O_{19}$ in grazing incidence geometry without field using right (σ_+) and left (σ_-) circularly polarised X-ray beams. The dotted lines represent the linear background. (b) Normalised XAS spectra and (c) XMCD signal.
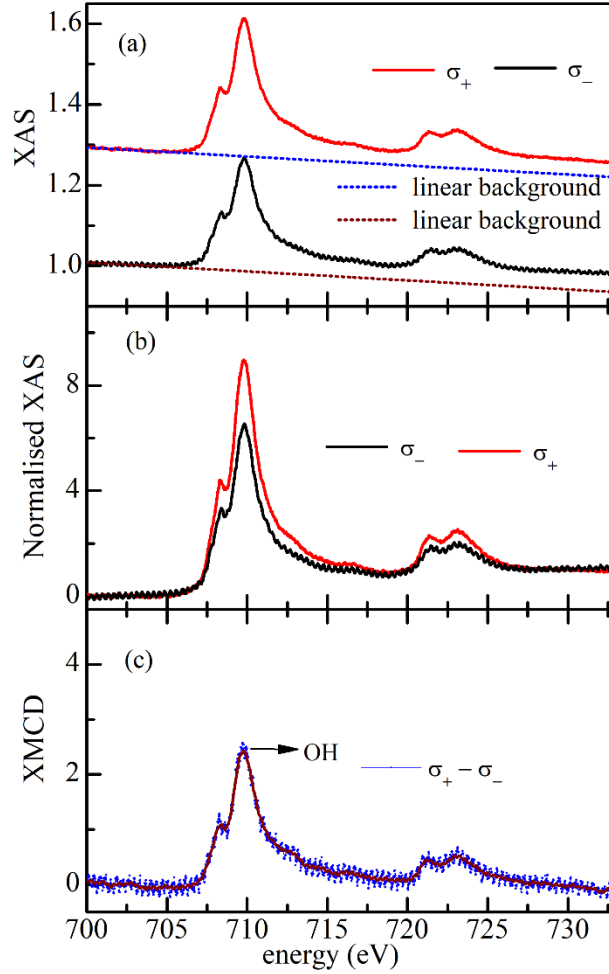
Figure 3.9: (a) XAS spectra recorded at the Fe $L_{2,3}$-edges measured at 1.2 K on a single-crystal of $BaFe_{12}O_{19}$ in grazing incidence geometry with field of 0.5 T using right (σ_+) and left (σ_-) circularly polarised X-ray beams. The dotted lines represent the linear background. (b) Normalised XAS spectra and (c) XMCD signal.

magnetic moment, n_h the number of $3dFe^{3+}$ holes in BFO. m_T^θ is related to the magnetic dipole operator and its contribution is negligible for $3dFe^{3+}$ [202]. To calculate spin magnetic moment in GI geometry using sum-rule, we need P, Q and R values. We followed the steps discussed in ref. [211] to estimate P, Q and R. We first obtained the summed XAS spectra (= $\sigma_+ + \sigma_-$). Then, we removed the edge jump using a two-step-like function. The height of the two-step-like function at peak position of L_3-edge and L_2-edge was set to 2/3 and 1/3 of average intensity of post edge of normalised Fe XAS spectra,

respectively. After removal of contribution of edge jump from summed XAS, we integrated the summed XAS spectra over the $L_{2,3}$ energy range. The variation of the XMCD signal integrated over the $L_{2,3}$ energy range and sum XAS with its integration are shown in Figs. 3.10(a) and (b), respectively, for H = 0. We estimated the value of P, Q and R using these two figures and then calculated the spin moment using Equation (3.2). We followed the same procedure to obtain the XMCD integration and XAS integration for H = 0.5 T and their variation over $L_{2,3}$ energy range has been depicted in Figs. 3.11(a) and (b), respectively. Using the P, Q and R values of GI geometry for H = 0 T and 0.5 T, we have calculated the parallel and perpendicular components of the moment. The calculated spin moments parallel to the c-axis for the zero-field (H = 0 T) and H = 0.5 T field are found to be $m_{spin//c} \sim 0.2009$ μ_B/Fe and ~ 0.56228 μ_B/Fe, respectively, while
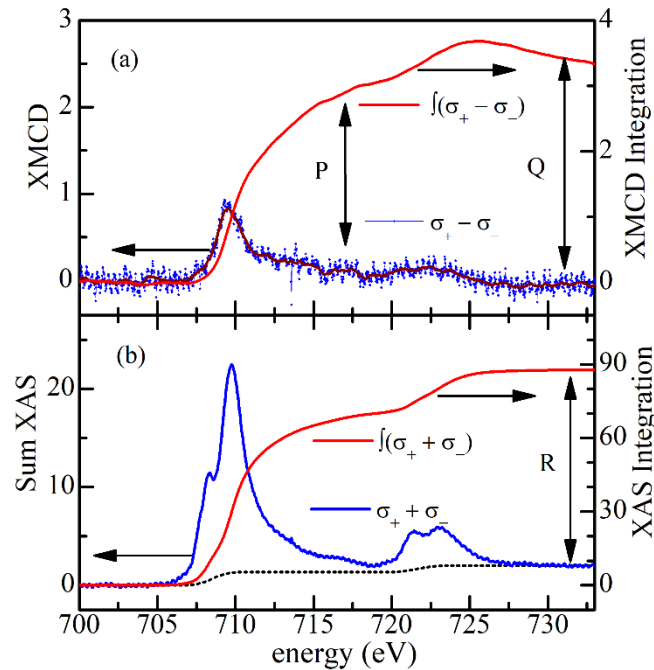

Figure 3.10: (a) The XMCD signal and (b) sum XAS along with their integration measured in grazing incidence geometry without field at 1.2 K. The dotted line in (b) is the two-step-like function used for edge jump removal before XAS integration.
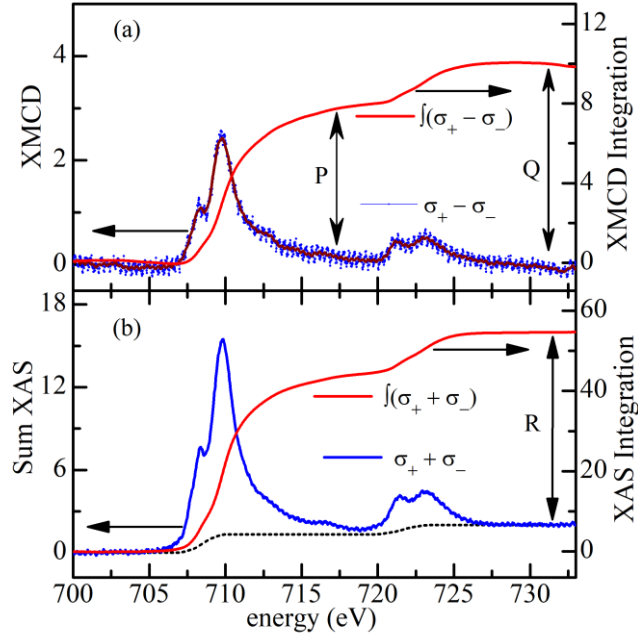
Figure 3.11: (a) The XMCD signal and (b) sum XAS along with their integration measured in grazing incidence geometry with field of 0.5 T at 1.2 K. The dotted line in (b) is the two-step-like function used for edge jump removal before XAS integration.

those perpendicular to the c-axis are $m_{spin\perp c}$ ~0.0538 μ_B/Fe and ~ 0.15058 μ_B/Fe, respectively. At 4 K, magnetic moments per Fe^{3+} ion in BFO is ~1.38 μ_B as estimated using single-crystal neutron diffraction study [15]. Further, magnetic moment of ~ 1.23 μ_B per Fe^{3+} in strontium hexaferrite has been reported using XMCD studies carried out on powder samples of $SrFe_{12}O_{19}$ at 2 K under a field of 6 T [202]. XMCD study under the same experimental condition on the hexagonal platelets of $SrFe_{12}O_{19}$, however, shows a moment of ~0.84 μ_B per Fe ion only. In the present case, XMCD study at 1.2 K under a field of 0.5 T gives $m_{spin//c}$ ~ 0.56228 μ_B per Fe ion which is quite reasonable in comparison to the reported value for the $SrFe_{12}O_{19}$ platelets. Application of magnetic field in the GI geometry obviously enhances the XMCD signal as well as $m_{spin\perp c}$ and $m_{spin//c}$ values, as expected due to better alignment of moments. A full alignment of the moments requires a magnetic field of ~ 2 T for H $\perp$ c and 1.5 T for H // c, as can be seen
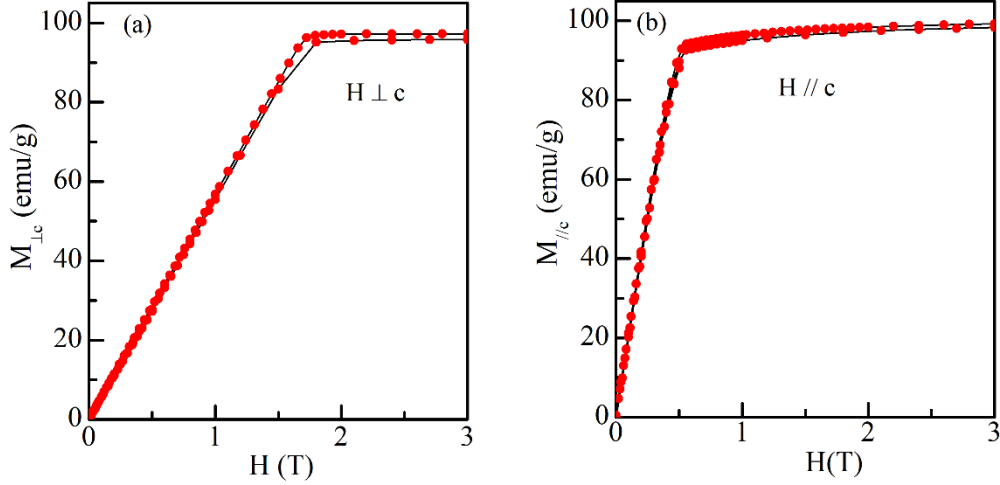
Figure 3.12: M-H curve measured at 2 K on single-crystal under various field applied (a) perpendicular and (b) parallel to the c-axis.

from the magnetization versus field curves recorded at 2 K shown in Fig. 3.12. This would have given us the value of magnetic moment close to the anticipated moment per Fe^{3+} of 1.38 μ_B. Notwithstanding the fact the observed moment using XMCD signal is lower than that anticipated for the monodomain crystal, non-zero significant magnetic moment $m_{spin \perp c}$ unambiguously confirms the non-Gorter type non-collinear magnetic structure of BFO at 1.2 K.

3.5.2 Neutron Diffraction Study at 1.5 K

The canted nature of the Fe^{3+} spins away from the c-axis in hexaferrites is known to lead to conical type magnetic order [3,29,101,102]. To verify this, we carried out single-crystal neutron diffraction studies at 1.5 K. As per the nuclear space group $P6_3/mmc$ of BFO, Bragg peaks for the *hhl* type reciprocal lattice rows with $l = 2n \pm 1$. These reflections are forbidden as per the collinear magnetic structure of the Gorter model with $P6_3/mm'c'$ magnetic space group also. The neutron diffraction pattern recorded along the *00l* reciprocal lattice row of BFO, however, reveals significant magnetic scattering around the *003* forbidden position (see Fig. 3.13) which clearly
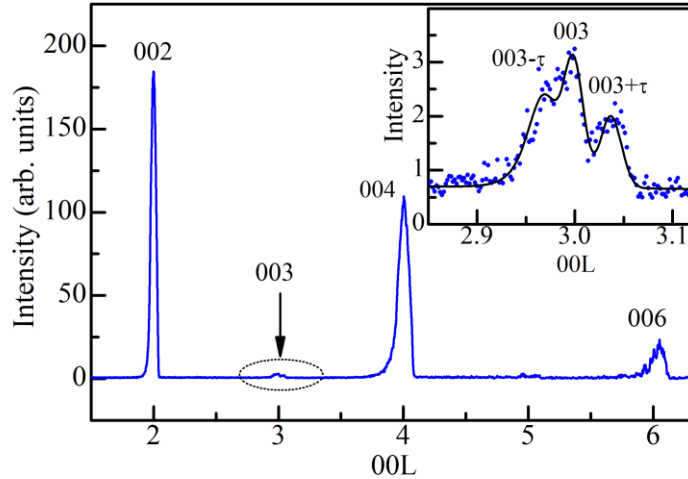
Figure 3.13: Single-crystal neutron diffraction pattern recorded along *00l* reciprocal lattice row at 1.5 K depicting a magnetic peak around *003* position. The inset shows the triplet character of the magnetic peak with reflections at $l = 3$ and $l = 003 - \tau_1$ and $003 + \tau_2$ positions.

confirms the non-collinear nature of the spins in BFO in agreement with the XMCD results. A careful analysis of the profile observed around *003* position reveals that it is a triplet consisting of one peak at *003* position and two satellite peaks (see the inset of Fig. 3.13).

The origin of the two satellites at nearly symmetrical position about *003* reflection has been explained in terms of the block-type conical magnetic structure of hexaferrites [29,132,133] where the magnetic unit cell is divided into two blocks, R and R′, as depicted in Fig. 3.1(a). Within each block, the magnetic spins are canted away from the c-axis in such a way that the net magnetic moment is collinear within the block but noncollinear with respect to the neighbouring block. The block-type longitudinal conical magnetic structure // to the c-axis is schematically illustrated in Fig. 3.1(c) where the net moment of each block precesses about the c-axis leading to the conical magnetic order with a half cone angle α. The angle ϕ shown in Fig. 3.1(c) is the phase difference between the ab-(basal) plane components of the net moments of the R and R′ blocks. It is given by

$\phi = \pi(1 - c/p)$ [132]. The propagation vector (k_0) of the longitudinal conical structure is along the c-axis of the unit cell.

The satellite peaks in Fig. 3.13 are not equally spaced with respect to the *003* peak. The satellite on the left and right side of *003* are located at $\tau_1 \simeq 0.034$. and $\tau_2 \simeq 0.045$ which give the periodicity ($p \sim c/\tau$) of the conical order as ~ 682 Å and ~ 515 Å, respectively. These periodicities are nearly 29 and 22 times the value of the c-parameter of the nuclear unit cell but are not exactly equal to 29c or 22c. The fact that $\tau_1 \neq \tau_2$ and the periodicity p is not a multiple of the c-parameter of BFO clearly suggest that the conical modulation in BFO is incommensurate with respect to the collinear magnetic lattice. In case of Sc doped BFO with x = 1.8, this periodicity is ~ 141 Å which is about 6 times the c-parameter [132]. The phase shift ϕ obtained by us for BFO is $\sim 174^0$ using τ_1 and $\sim 172^0$ using τ_2, as compared to $\sim 150^0$ for Sc doped BFO [132]. When the phase shift ϕ for the ab-components of the net moments of the R and R′ blocks becomes 180^0, it leads to the appearance of screw-type spin structure [132] whose pitch is equal to the c-parameter of the nuclear unit cell. As a result of such an antiparallel arrangement of the ab-plane components, new magnetic reflections appear at $l = 2n \pm 1$ position along the *00l* reciprocal lattice row. We also observe such a reflection as shown in the inset of Fig. 3.13 for *003*. However, in the present case, the *003* peak is most likely due to multiple scattering as we do not see significant intensity at *005* position even though the satellite peaks are present. The presence of the *003* reflection along with the two satellite peaks at *003* - τ_1 and *003* + τ_2 shown in the inset of Fig. 3.13 confirms the existence of the conical type structure in the ground state of BFO even though the longitudinal conical modulation is incommensurate with respect to the underlying lattice. The presence of these satellites also confirms the non-collinear magnetic structure of BFO.

3.6   Conclusions

(1). We have presented evidence for the non-collinear magnetic structure of BFO using XAS and XMCD studies at 1.2 K.

(2). Single-crystal neutron diffraction measurements at 1.5 K along the *00l* reciprocal lattice row reveal magnetic satellite peaks at *003* - τ_1 and *003* + τ_2 positions which are forbidden by the nuclear $P6_3/mmc$ and magnetic $P6_3/mm'c'$ space groups for the collinear Gorter model. This provides additional confirmation of the non-collinear magnetic structure of BFO in its ground state.

(3). The magnetic satellite peaks at *003* - τ_1 and *003* + τ_2 observed by us are due to longitudinal conical type magnetic structure in the ground state of BFO at T $\lesssim$ 1.5 K. Since the satellites are not equally spaced with respect to the *003* position and, hence, give different periodicities of the conical order (~ 682 Å and ~ 515 Å), which are not an integral multiple of the c-parameter, the conical modulation is incommensurate with respect to the underlying collinear magnetic structure of BFO.

(4). Our observations provide the basis for the existence of magnetoelectric coupling under transverse field (H $\perp$ c) in BFO also, similar to that observed in Y- and Z-type hexaferrites.